Quest Journals
Journal of Research in Environmental and Earth Sciences
Volume 8 ~ Issue 7 (2022) pp: 25-31
ISSN(Online) :2348-2532
www.questjournals.org

Research Paper

Synthesis and application of $NiAl_2O_4/Al_2O_3$ nanocomposite Photocatalysts for wastewater treatment

Arup Dhara*
Department of Physics, Burdwan Raj College, Burdwan 713104, West Bengal, India.

Abstract
Spinel nickel aluminate ($NiAl_2O_4$) is synthesized by mechanical alloying the stoichiometric mixture of NiO and Al_2O_3 powders followed by annealing the milled powders at 950 ℃. The synthesized compound is also characterized by XRD and UV-vis spectra analyses. The UV-vis spectra indicate the presence of a small amount of Al_2O_3 in the synthesized sample. The photocatalytic degradation of Rhodamine B (RhB) dye in an aqueous solution in presence of $NiAl_2O_4/Al_2O_3$ nanocomposite is found to be ~ 82 % under visible light irradiation. The photocatalytic performance of the material indicates that it can be used for the removal of organic pollutants from wastewater.

Keywords: *$NiAl_2O_4$ spinel; Nanocomposite; Wastewater; Photocatalysts.*

***R**eceived 03 July, 2022; **R**evised 13 July, 2022; **A**ccepted 18 July, 2022 © The author(s) 2022.*
P**ublished with open access at **www.questjournals.org

I. Introduction

Both metal oxides and mixed metal oxides are being extensively used in different fields such as optics[1,2], electronics[3,4], catalysis[5,6], and so on. A spinel compound is a mixed cation ternary oxide material whose physicochemical properties mainly depend on the cationic distributions among the tetrahedral and octahedral sites in the crystal lattice [7–9]. The ideal spinel structure consists of a cubic close-packed array of anions with one-eighth of the tetrahedral and half of the octahedral sites occupied by Ni^{2+} and Al^{3+} cations [9,10]. Cubic nickel aluminate ($NiAl_2O_4$) spinel belongs to the space group $Fd\bar{3}m$and with normal spinel structure. The $NiAl_2O_4$ ($NiO\text{-}Al_2O_3$) binary oxide system has various interesting applications in the field of catalysts[5,6], anode material for SOFC[11], and chemical-looping combustion[12,13]. Generally, the optical and structural properties of nanomaterials are very different from their bulk counterparts. The effects of temperature and pressure on the cations distribution in $NiAl_2O_4$ and its applications as catalysts have been studied over the years by different authors and methods. There are many synthesis methods of $NiAl_2O_4$ nanocrystalline spinel, like solid-state reaction [9,14], mechanical alloying[15,16], microwave heating [17,18], microwave combustion method [19], sol-gel[20], co-precipitation[21]. Nazemi et al.[15] prepared nanostructure $NiAl_2O_4$ spinel from NiO and Al_2O_3 powders after 60h ball milling. They also found that 15h ball milling and 2h of heat treatment at 1100℃ was enough to prepare a single-phase nanostructure $NiAl_2O_4$ spinel. Han et al.[22] prepared nanostructure $NiAl_2O_4$ spinel from NiO and Al_2O_3 powders after 168h of ball milling. But, such a long-duration synthesis of the material is time-consuming and not suitable for industrial applications. Javanmardi et al.[16] prepared $NiAl_2O_4$ spinel by 5h mechanical milling the $NiCO_3$ and Al mixtures with subsequent annealing at 900℃ for 2h. The most general synthesis method of crystalline $NiAl_2O_4$ spinel is a solid-state reaction that involves the mixture of metal oxides and is usually performed at high temperatures. It is the simplest synthesis process but in this method, it is difficult to synthesize stoichiometric $NiAl_2O_4$ as even the starting mixture contains a critical 1:1 molar ratio in NiO and Al_2O_3.[22] Han et al.[22] proposed some points by which one can reduce the excess reactants in the desired single-phase $NiAl_2O_4$ spinel sample. Cooley and Reed[23] prepared a nickel aluminate spinel with NiO excess even heating it at 1391℃ for 2 days. The use of higher temperature to improve the crystallinity of the $NiAl_2O_4$ spinel phase is the main drawback and also unavoidable [24]. The crystal formation and growth mechanism of $NiAl_2O_4$ depend on the cation counter diffusion at the interface of both metal oxides NiO and Al_2O_3 during the initial stage of the thermal treatment. Very high energy is required to speed up the counter diffusion process; thus the formation of $NiAl_2O_4$ usually happens at higher temperatures. The diffusion of Ni^{2+} ions at the Al_2O_3 interface leads to the formation of Al^{3+} ions (Eq. 1) which diffuses at the interface of NiO and forms Ni^{2+} ions (Eqn.2) and vice versa. These two processes (Eq.1 and Eq.2) occur simultaneously and are equivalent to the overall Eq.3.[24,25]

*Corresponding Author: Arup Dhara

At Al_2O_3 interface:

$$3Al_2O_3 + 2Ni^{2+} \rightarrow 2NiAl_2O_4 + 2Al^{3+} + 0.5O_2 \quad (1)$$

At NiO interface:

$$2Al^{3+} + 3NiO + 0.5O_2 \rightarrow NiAl_2O_4 + 2Ni^{2+} \quad (2)$$

The overall reaction:

$$Al_2O_3 + NiO \rightarrow NiAl_2O_4 \quad (3)$$

So it is desirable that if the area of the interface of both metal oxides increases; it will boost up the counter diffusion phenomenon and as a result, the formation of the crystalline $NiAl_2O_4$ phase may occur at a comparatively lower temperature. By keeping this fact in mind, in the present study, an attempt has been made to synthesize stoichiometric nanocrystalline $NiAl_2O_4$ spinel by the mechanical alloying of NiO and Al_2O_3 powders followed by annealing the milled powders at 950℃. The aims of this study are (i) synthesis of $NiAl_2O_4$ nanocrystals by mechanical alloying followed by solid-state reaction and (ii) to examine the photocatalytic efficiency of the synthesized material under visible light irradiation.

II. Experimental section

2.1 Synthesis of $NiAl_2O_4/Al_2O_3$ nanoparticles

The homogeneous stoichiometric mixture (1:1 molar ratio) of nickel oxide (99%, Sigma-Aldrich) and aluminum oxide (99%, Merck) powders were prepared by hand grinding the accurately weighed powders in an agate mortar for 30 min. The mixture was then placed into a tungsten carbide vial containing 30 tungsten carbide balls. Mechanical alloying of the mixture was carried out for 4h in a dry medium by a high-energy planetary ball mill (P6, M/S Fritsch, GmbH, Germany). Precautions were taken to avoid any inclusion of impurity from the milling media. For annealing in the open air, a part of the milled powders was placed in a muffle furnace set at 950°C with a constant heating rate of 5 K min^{-1}. The sample was heated for 5h and then cooled in air.

2.2 Characterizations of synthesized $NiAl_2O_4/Al_2O_3$ nanocomposite

X-ray diffraction (XRD) data of the synthesized powders were recorded by an automated (Bruker AXS, D8 Advance, Da Vinci) X-ray diffractometer with Ni-filtered CuK_α radiation $\lambda = 1.5418$ Å. For the UV-visible absorption study, a small amount of the powder sample was fairly dispersed in ethanol using vigorous sonication and then the solution was transferred to a quartz cuvette of the spectrophotometer. The UV-visible absorption spectra of the nanocomposite were recorded in a UV–vis spectrophotometer (Shimadzu UV-1800, Japan) within the wavelength range of 200–800 nm.

The photocatalytic performance of $NiAl_2O_4/Al_2O_3$ nanocomposite was studied by the photodegradation of model organic pollutant Rhodamine B (RhB) dye under the visible light (200W tungsten lamp, λ>420nm) irradiation at room temperature. A 150 ml of an aqueous solution of 10mg/L RhB was placed in a glass beaker and then 3mg of the photocatalyst was added to the solution. The mixture was then magnetically stirred in dark for 30 min to reach desorption-adsorption equilibrium before light illumination. The blank experiment (without photocatalyst) and dark experiment (without light) were also carried out for the same period as the photocatalytic experiment. During the process of reaction, the upper clear solution was analyzed every 30 min by recording the maximum absorption band (553 nm for RhB) in the successively UV-visible spectra using a Shimadzu UV-1800 spectrophotometer.

III. Results And Discussion

3.1 XRD analysis

Fig.1 represents the XRD patterns of the unmilled NiO + γ-Al_2O_3 (1:1 mol %) powder mixture, 4h ball-milled powder mixture, and 4h ball-milled powder annealed at 950℃ for 5h. The presence of crystalline phases in the compounds is identified from the respective JCPDS databases. The XRD pattern of the unmilled sample comprises the individual reflections from both NiO (JCPDS: # 04-0835) and γ-Al_2O_3 (JCPDS: #10- 0425) phases. The most intense peak of γ-Al_2O_3 is located at $2\theta = 67.093^{26}$. It is obvious from Fig.1 that after 4hof ball milling, the growth of the spinel $NiAl_2O_4$ phase is initiated in presence of the precursor phases. The XRDpattern of the annealed sample (at the top of Fig.1) contains all the reflections from the $NiAl_2O_4$ phase (#JCPDS: 10-0339).

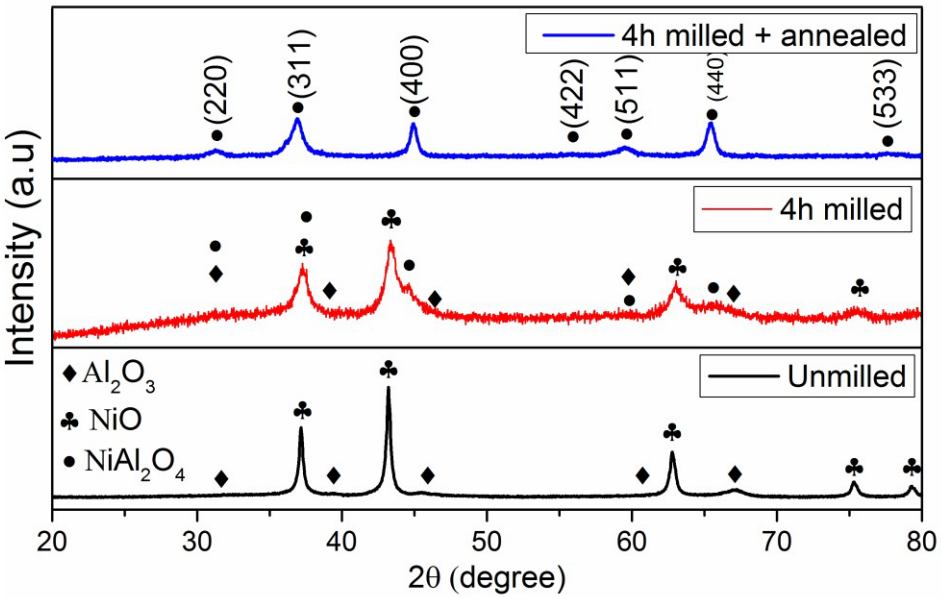

Fig.1 XRD patterns of the unmilled, 4h milled and 4h milled powder annealed at 950 ℃ samples

3.2 UV-vis absorption study

To estimate the energy band gap value of the prepared sample, the optical absorption spectrum has been obtained from a UV-vis spectrometer. Fig.2 shows the absorption spectrum of the sample and depicts that the material can absorb radiation in the ultraviolet range as well as visible range in the spectral region of 200-800 nm. The precise optical band gap value of the sample is evaluated from the UV-Vis spectrum by using the Tauc relation:[27,28]

$$(\alpha h\nu)^{1/n} = A\,(h\nu - E_g) \qquad (4)$$

where α is the absorption coefficient, $h\nu$ is the incident photon energy, A is a constant and E_g is the band gap energy of the material. The exponent 'n' depends on the type of the transition. For a direct band gap semiconductor, the value of the exponent is taken to be $\frac{1}{2}$. The band gap energy has been calculated by extrapolating the linear portions of the $(\alpha h\nu)^2$ vs hν plot on the $h\nu$ axis. From the slope of the Tauc plot (inset of Fig. 2), two band gap values are estimated. The band gap values 2.90 eV and 3.91 eV belong to $NiAl_2O_4$ nanocrystallites [29,30] and γ-Al_2O_3 nanocrystallites [31] respectively and these estimated values are well consistent with the previously reported values. This finding indicates that there may exist a small amount of Al_2O_3 present in the synthesized sample.

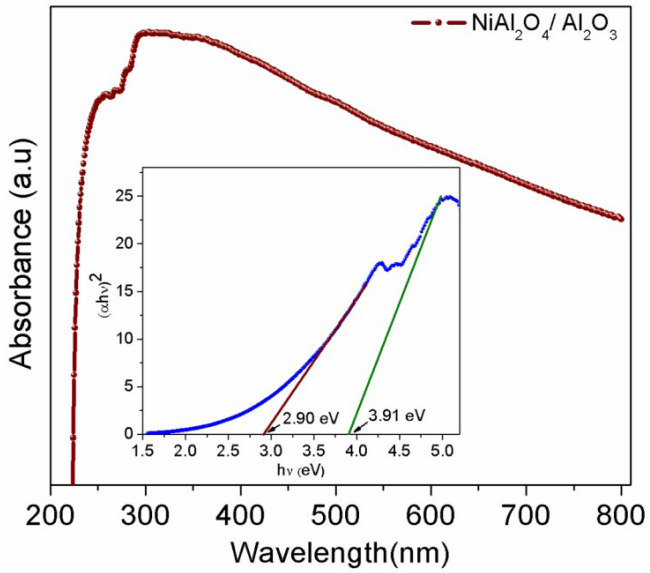

Fig.2: Optical absorption spectrum of $NiAl_2O_4/Al_2O_3$ nanocomposite

3.3 Photocatalytic activity

Dyes are one of the most used chemical compounds in industries. The excessive presence of these compounds in wastewater causes dangerous consequences to nature's surroundings. Rhodamine B (RhB) is one of the most used model dyes in photocatalytic experiments. The synthesized $NiAl_2O_4/Al_2O_3$ photocatalyst has been used to explore the degradation of the RhB dye under visible light (λ > 420 nm) irradiation at room temperature and the corresponding result is shown in Fig.3.

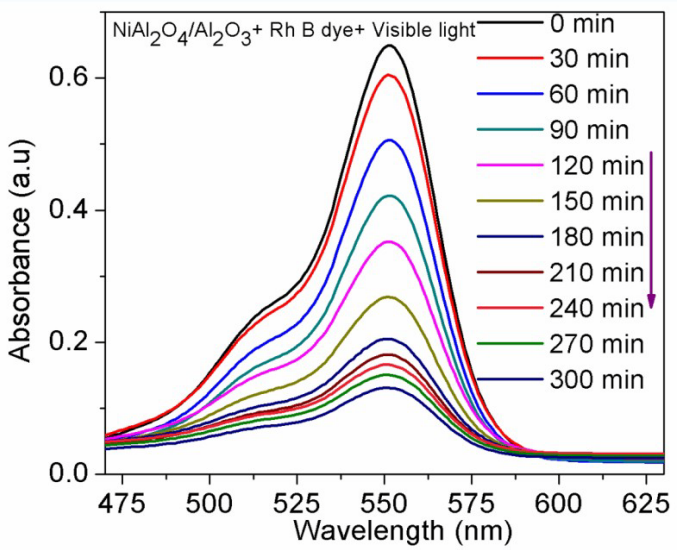

Fig.3: Time dependant UV-vis absorption spectra of RhB aqueous solution in the presence of $NiAl_2O_4/Al_2O_3$ nanocomposite, as a function of irradiation time.

Fig. 4 shows the photocatalytic degradation of the RhB dye within 300 min under visible light irradiation in the presence of $NiAl_2O_4/Al_2O_3$ nanocomposite. The decolorization of RhB solution is strongly activated by the presence of the $NiAl_2O_4/Al_2O_3$ photocatalyst under the irradiation of visible light. It is also clear from the plot that the photocatalyst is the main key factor for the degradation. The percentage of the degradation efficiency (η) of the RhB dye has been calculated as,

$$\eta = \frac{C0-C}{C_0} \text{ x } 100\% \quad (5)$$

The degradation efficiency of ~50% were obtained within 120 min visible light irradiation. The degradation of all organic dyes increases with increasing irradiation time and follows the pseudo-first-order kinetics.
The photocatalytic reaction is assumed to follow Langmuir–Hinshelwood (L–H) kinetic model:[27,28]

$$\ln(\frac{C}{C_0}) = -k.t \quad (6)$$

where 'k' is the reaction rate constant (min^{-1}), C_0 is the initial concentration (at t=0) and C is the residual concentration of dye after a certain time 't' (min). The degradation rate constant 'k' was calculated from the slope of the kinetic plot (Fig.5) which shows two different values of 'k'. Initially, up to 180 min, the 'k' value is 0.0071 min^{-1} and then the value becomes 0.0037 min^{-1}.

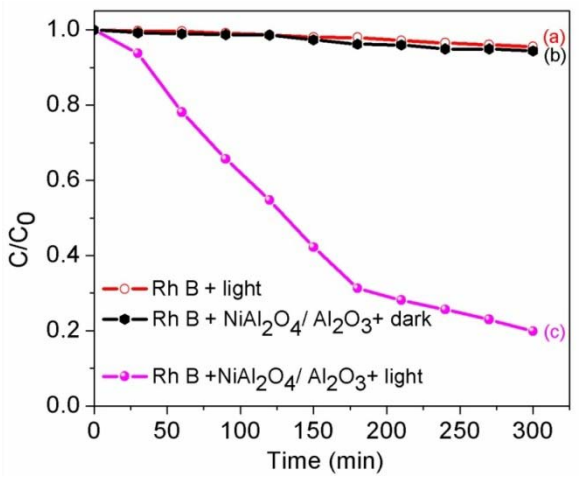

Fig.4: Plot of C/C_0 versus irradiation time

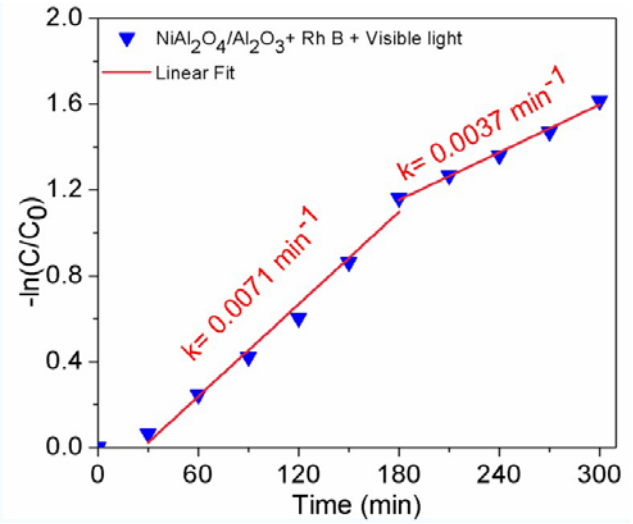

Fig.5. The plot of $-\ln(C/C_0)$ as a function of irradiation time

3.3.1 Photocatalytic mechanism and performance

Based on the above results, a possible mechanism of the enhanced photocatalytic performances of RhB dye pollutant with $NiAl_2O_4/Al_2O_3$ nanocomposite is proposed and shown in Fig.6. In photodegradation, the pollutants are oxidized by some reactive species such as hydroxyl radicals ($OH^{\bullet}$), holes (h^+) and superoxide radicals ($O_2^{\bullet-}$).[27,28,32] It is already established that hydroxyl radicals ($OH^{\bullet}$) generated by the illumination of the photocatalyst are the main species responsible for the photocatalytic degradation of organic pollutant molecules. As Al_2O_3 has no absorption response to visible light due to its wide band gap energy, the visible light absorption of $NiAl_2O_4/Al_2O_3$ nanocomposite is solely contributed by the $NiAl_2O_4$ component in the photocatalytic reaction. Under visible light illumination, electron-hole pairs are generated on $NiAl_2O_4$. The band-edge position plays a significant role in determining the photoexcited charge carriers capturing to produce different reactive species. The conduction band-edge potential (E_{CB}) and valance band-edge potential (E_{VB}) of $NiAl_2O_4$ have been estimated by using this empirical formulie:[28,32]

$$E_{CB} = X - E^e - 0.5\, E_g \quad (7)$$

$$E_{VB} = E_{CB} + E_g \quad (8)$$

where X, E^e, and E_g are the absolute electronegativities, the energy of free electrons on the hydrogen scale (4.5 eV), and the band gap energy of the semiconductor respectively. The absolute electronegativity (X) of $NiAl_2O_4$ is calculated by the geometric mean of the absolute electronegativity of the constituent atoms. The absolute electronegativity of the constituent atoms is defined as the arithmetic mean of the atomic electron affinity and first ionization energy of the individual atoms. The X value and the band gap energy for $NiAl_2O_4$ are 5.46 eV and 2.90 eV respectively. The E_{CB} and E_{VB} of $NiAl_2O_4$ are calculated as -0.41 eV and 2.49 eV respectively. The conduction band potential of $NiAl_2O_4$ (-0.41 eV) is more negative than the oxidation potential of $O_2/\dot{O}_2^-$ (-0.33 eV), hence photogenerated electrons react with the dissolved O_2 molecule in the solution to produce $\dot{O}_2^-$. The

RhB dye could be photodegraded via the reaction with $\dot{O}_2^-$. The potential for O_2 /H_2O_2 (0.695 eV) is higher than the CB potential of $NiAl_2O_4$ (-0.41 eV). Thus, the electrons in the CB of $NiAl_2O_4$ react with absorbed O_2 to generate H_2O_2. Afterward, this produces $OH^\bullet$ radical by capturing electrons. On the other hand, the oxidation of H_2O to hydroxyl radical does not occur due to the higher potential of H_2O/ $OH^\bullet$ (2.8 eV) than the VB potential of $NiAl_2O_4$ (2.41 eV). But, the VB potential is higher than the oxidation potential of OH^-/ $OH^\bullet$ (2.38 eV), as a result, the oxidation of OH^- to hydroxyl radical takes place by capturing photogenerated holes.

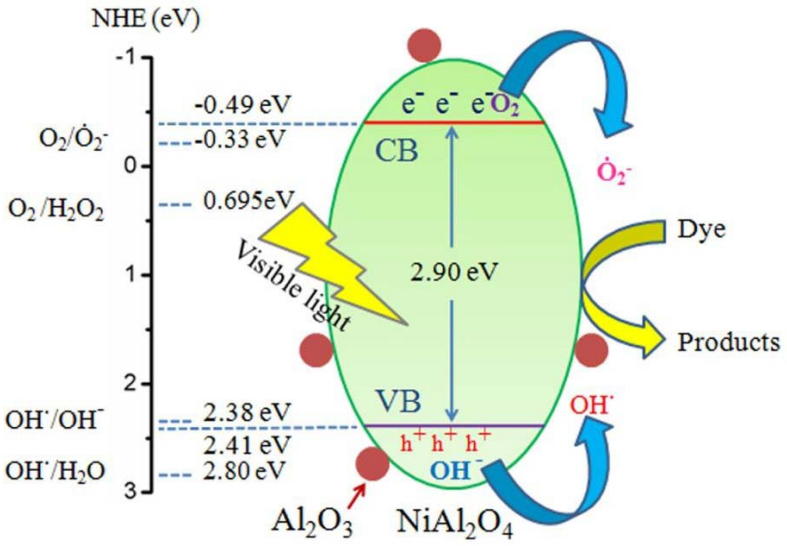

Fig.6. Proposed photodegradation mechanism of RhB dye in presence of $NiAl_2O_4/Al_2O_3$ nanocomposite photocatalyst

Accordingly, the photogenerated holes react directly with absorbed dye pollutant molecules to produce degraded products. The whole mechanism of photocatalytic reactions can be summarized with the following equations (9-16):

$$NiAl_2O_4/Al_2O_3 + h\nu \text{ (visible light)} \rightarrow e^-_{CB}\ (NiAl_2O_4) + h^+_{VB}\ (NiAl_2O_4) \quad (9)$$

$$e^-_{CB}\ (NiAl_2O_4) + O_2 \rightarrow \dot{O}_2^- \quad (10)$$

$$\dot{O}_2^- + RhB \rightarrow \text{degraded products} \quad (11)$$

$$2e^-_{CB}\ (NiAl_2O_4) + 2H^+ + O_2 \rightarrow H_2O_2 \quad (12)$$

$$H_2O_2 + e^-_{CB}(NiAl_2O_4) \rightarrow OH^- + OH^\bullet \quad (13)$$

$$OH^- + h^+_{VB}\ (NiAl_2O_4) \rightarrow OH^\bullet \quad (14)$$

$$OH^\bullet + RhB \rightarrow \text{degraded products} \quad (15)$$

$$h^+_{VB}\ (NiAl_2O_4) + RhB \rightarrow \text{degraded products} \quad (16)$$

Several reasons may account for the enhanced photocatalytic activity of the $NiAl_2O_4/Al_2O_3$ photocatalyst, (i) due to the amphoteric nature of the Al_2O_3, it is insoluble in water and forms a layer on the $NiAl_2O_4$ surface can effectively protect the $NiAl_2O_4$ from dissolution in aqueous solution[33], (ii) the specific surface area of the $NiAl_2O_4$ nanoparticles increased by ball milling, so both adsorptions and catalytic performances are enhanced considerably and (iii) the non-semiconducting Al_2O_3 nanoparticles serve as surface additives which facilitate the trapping of photoinduced carriers[34].

IV. Conclusions

In the present study, we have synthesized $NiAl_2O_4/Al_2O_3$ nanocomposite by mechanical alloying followed by sintering at a comparatively lower temperature at 950 ℃ than usual. The band gap energies of major $NiAl_2O_4$ and minor γ-Al_2O_3 phases are found to be 2.90 eV and 3.91 eV respectively. $NiAl_2O_4/Al_2O_3$ nanocomposite photocatalyst exhibits enhanced photocatalytic activity under visible light irradiation. The photocatalytic degradation of RhB dye in presence of $NiAl_2O_4/Al_2O_3$ nanocomposite is found to be ~ 82 %. The insolubility of γ-Al_2O_3 effectively protects $NiAl_2O_4$ spinel from dissolution. These findings indicate that the synthesized $NiAl_2O_4/Al_2O_3$ nanocomposite may provide a new approach for high-performance photocatalyst design and several environmental issues.

Acknowledgment

The author wishes to thank Prof. S.K. Pradhan who provided me an opportunity to access the laboratory and research facilities at the material Science lab., Department of Physics, The University of Burdwan.

References

[1]. D. F. Ogletree, P. J. Schuck, A. F. Weber-bargioni, N. J. Borys, S. Aloni, W. Bao, S. Barja, J. Lee, M. Melli, K. Munechika, S. Whitelam and S. Wickenburg, *Advanced Materials*, 2015, **27**, 5693–5719.
[2]. J. Li and J. Z. Zhang, *Advanced Materials*, 2015, **27**, 3015–3041.
[3]. X. Yu, T. J. Marks and A. Facchetti, *Chemical Review*, 2010, **110**, 383–396.
[4]. D. V Talapin, J. Lee, M. V Kovalenko and E. V Shevchenko, *Chemical Review*, 2010, **110**, 389–458.
[5]. N. Sahli, C. Petit, A. C. Roger, A. Kiennemann, S. Libs and M. M. Bettahar, *Catalysis Today*, 2006, **113**, 187–193.
[6]. A. Srifa, R. Kaewmeesri, C. Fang, V. Itthibenchapong and K. Faungnawakij, *Chemical Engineering Journal*, 2018, **345**, 107–113.
[7]. B. Antic, A. Kremenović, A. S. Nikolic and M. Stoiljkovic, *Journal of Physical Chemistry B*, 2004, **108**, 12646–12651.
[8]. M. Vucinic-Vasic, E. S. Bozin, L. Bessais, G. Stojanovic, U. Kozmidis-Luburic, M. Abeykoon, B. Jancar, A. Meden, A. Kremenovic and B. Antic, *Journal of Physical Chemistry C*, 2013, **117**, 12358–12365.
[9]. Y. S. Han, J. B. Li, X. S. Ning and B. Chi, *Journal of the American Ceramic Society*, 2005, **88**, 3455–3457.
[10]. A. Ray, A. Roy, M. Ghosh, J. A. Ramos-ramón and S. Saha, *Applied Surface Science*, 2019, **463**, 513–525.
[11]. A. Reyes-Rojas, H. E. Esparza-Ponce and J. Reyes-Gasga, *Journal of Physics Condensed Matter*, 2006, **18**, 4685–4696.
[12]. H. Zhao, L. Liu, B. Wang, D. Xu, L. Jiang and C. Zheng, *Energy and Fuels*, 2008, **22**, 898–905.
[13]. E. Jerndal, T. Mattisson, I. Thijs, F. Snijkers and A. Lyngfelt, *International Journal of Greenhouse Gas Control*, 2009, **94**, 665–676.
[14]. F. S. PETTIT, E. H. RANDKLEV and E. J. FELTEN, *Journal of the American Ceramic Society*, 1966, **49**, 199–203.
[15]. M. K. Nazemi, S. Sheibani, F. Rashchi, V. M. Gonzalez-Delacruz and A. Caballero, *Advanced Powder Technology*, 2012, **23**, 833–838.
[16]. M. JAVANMARDI, R. EMADI and H. ASHRAFI, *Transactions of Nonferrous Metals Society of China (English Edition)*, 2016, **26**, 2910–2915.
[17]. M. Mohammadpour Amini and L. Torkian, *Materials Letters*, 2002, **57**, 639–642.
[18]. R. D. Peelamedu, R. Roy and D. K. Agrawal, *Materials Letters*, 2002, **55**, 234–240.
[19]. S. Jayasree, A. Manikandan, S. A. Antony, A. M. Uduman Mohideen and C. Barathiraja, *Journal of Superconductivity and Novel Magnetism*, 2016, **29**, 253–263.
[20]. B. Gunduz, A. A. Al-Ghamdi, A. A. Hendi, Z. H. Gafer, S. El-Gazzar, F. El-Tantawy and F. Yakuphanoglu, *Superlattices and Microstructures*, 2013, **64**, 167–177.
[21]. S. Kurien, J. Mathew, S. Sebastian, S. N. Potty and K. C. George, *Materials Chemistry and Physics*, 2006, **98**, 470–476.
[22]. Y. S. Han, J. B. Li, X. S. Ning, X. Z. Yang and B. Chi, *Materials Science and Engineering A*, 2004, **369**, 241–244.
[23]. R. F. Cooley and J. S. Reed, *Journal of the American Ceramic Society*, 1972, **55**, 395–398.
[24]. A. A. S. Gonçalves, M. J. F. Costa, L. Zhang, F. Ciesielczyk and M. Jaroniec, *Chemistry of Materials*, 2018, **30**, 436–446.
[25]. N. M. Deraz, *International Journal of Electrochemical Science*, 2013, **8**, 5203–5212.
[26]. R. H. R. Castro and D. V Quach, *Physical chemistry C*, 2012, **116**, 24726–24733.
[27]. and A. K. A.Ganguly, O. Anjaneyulu, K.Ojha, K.Ganguli, *CrystEngComm*, 2015, **17**, 8978–9001.
[28]. and A. K. A.Ganguly, O. Anjaneyulu, K.Ojha, K.Ganguli, *CrystEngComm*, 2015, **17**, 8978–9001.
[29]. M. Rahimi-nasrabadi, F. Ahmadi and M. Eghbali-arani, *Journal of Materials Science: Materials in Electronics*, 2017, **28**, 2415–2420.
[30]. M. Maddahfar, M. Ramezani and M. Sadeghi, *Journal of Materials Science: Materials in Electronics*, 2015, **26**, 2–7.
[31]. H. Search, C. Journals, A. Contact and M. Iopscience, *Journal of Physics Condensed Matter*, 2004, **16**, 2891–2900.
[32]. and A. K. A.Ganguly, O. Anjaneyulu, K.Ojha, K.Ganguli, *CrystEngComm*, 2015, **17**, 8978–9001.
[33]. K. Z. Zhang L, Zhang H, Huang H, Liu Y, *New journal of chemistry*, 2012, **36**, 1541–1544.
[34]. X. Fu, W. Tang, L. Ji and S. Chen, *Chemical Engineering Journal*, 2012, **180**, 170–177.